Structural, defect, transport and dopant properties of AgNbO3

Kuganathan, N. & Chroneos, A.

Author post-print (accepted) deposited by Coventry University's Repository

Original citation & hyperlink:
Kuganathan, N & Chroneos, A 2020, 'Structural, defect, transport and dopant properties of AgNbO3', Chemnanomat, vol. 6, no. 9, pp. 1337-1345. https://dx.doi.org/10.1002/cnma.202000327

DOI 10.1002/cnma.202000327
ISSN 2199-692X

Publisher: Wiley

This is the peer reviewed version of the following article: Kuganathan, N & Chroneos, A 2020, 'Structural, defect, transport and dopant properties of AgNbO3', Chemnanomat, vol. 6, no. 9, pp. 1337-1345., which has been published in final form at https://dx.doi.org/10.1002/cnma.202000327. This article may be used for non-commercial purposes in accordance with Wiley Terms and Conditions for Self-Archiving.

Copyright © and Moral Rights are retained by the author(s) and/ or other copyright owners. A copy can be downloaded for personal non-commercial research or study, without prior permission or charge. This item cannot be reproduced or quoted extensively from without first obtaining permission in writing from the copyright holder(s). The content must not be changed in any way or sold commercially in any format or medium without the formal permission of the copyright holders.

This document is the author's post-print version, incorporating any revisions agreed during the peer-review process. Some differences between the published version and this version may remain and you are advised to consult the published version if you wish to cite from it.

Structural, defect, transport and dopant properties of $AgNbO_3$

Navaratnarajah Kuganathan[a],[b]*, Alexander Chroneos[a],[b]

[a] Dr. Navaratnarajah Kuganathan, Prof. Alexander Chroneos
Department of Materials, Imperial College London, London, SW7 2AZ, United Kingdom; n.kuganathan@imperial.ac.uk (N.K), alexander.chroneos@imperial.ac.uk (A.C)
[b] Dr. Navaratnarajah Kuganathan, Prof. Alexander Chroneos
Faculty of Engineering, Environment and Computing, Coventry University, Priory Street, Coventry CV1 5FB, United Kingdom; ad0636@coventry.ac.uk (N.K), ab8104@coventry.ac.uk (A.C)

*Corresponding Author: Navaratnarajah Kuganathan (ad0636@coventry.ac.uk)

Abstract

Silver niobate ($AgNbO_3$) is a candidate lead-free piezoelectric materials with potential applications in electronic technology and catalysis. Atomistic simulation techniques are used to examine the defects, diffusion of Ag^+ and O^{2-} ions, solution of dopants and electronic structures of pristine and doped configurations in $AgNbO_3$. The Ag Frenkel is the most favourable intrinsic defect leading to the formation of Ag vacancies that can vehicle self-diffusion of Ag^+ ions in this material. The calculated activation energy for the diffusion of O^{2-} ions (1.07 eV) is significantly lower than that calculated for the diffusion of Ag^+ ions (2.44 eV). The prominent isovalent dopants on the Ag and the Nb sites are found to be Na^+ and Ta^{5+} respectively. Doping of Ge on the Nb site can facilitate the formation of oxygen vacancies required for the oxygen diffusion. Additional Ag vacancies required for the self-diffusion of silver can be introduced by doping of Ca on the Ag site. Electronic structures of non-defective and defective $AgNbO_3$ are discussed using density functional theory calculations.

Keywords: $AgNbO_3$; defects; diffusion; dopants; atomistic simulation

1. Introduction

There is considerable interest in synthesising lead-free piezoelectric materials in order to reduce the level of environmental pollution arising from lead [1,2]. The perovskite silver niobate ($AgNbO_3$) is a candidate material for the preparation of lead-free ferroelectric $AgNbO_3$–based materials and its alloys with other perovskites have attracted considerable interest for use as a piezoelectric material in numerous electronic devices such as capacitors, medical ultrasound tomography and ferroelectric memories [3-5]. In order to enhance its application in photocatalysis and ferroelectric devices, a number of dopants have been experimentally considered [6-10]. In particular, Li *et al*. [11] prepared La-doped $AgNbO_3$ solid solution experimentallty and observed an improvement in the photocatalytic activity. Doping of Li on the Ag site was studied by Fu *et al*. [6] and it was determined that the increase of Li-concentration resulted an enhancement in the ferroelectricity. Furthermore, Ta-doped $AgNbO_3$ has been shown to be a good candidate material for high power energy storage devices [12].

Though there are a few experimetal studies on the doping of $AgNbO_3$ available in the literature, there are no systemetic theoretical studies considering dopants in this material. Computer modelling can provide useful information about promising dopants with preferred sites and charge compensation mechanisms [13-20]. The calculated solution energies would enable to predict promising dopants and comment on the existing experimental studies on doping in $AgNbO_3$. Furthermore, defect and diffusion properties are also important as they can impact the properties of the material.

In this study, a computational simulation study of defects, self-diffusion of silver and oxygen, doping of $AgNbO_3$ by isovalent (Li, Na, K, Rb and Ta) and aliovalent (Mn,

Ni, Zn, Co, Ca, Sr, Ba, Al, Ga, Sc, Y, Gd, La, Si, Ge, Ti, Sn, Zr and Ce) dopants and the electronic structures of doped configurations are examined.

2. Results and discussion

2.1. Crystal structure of $AgNbO_3$

The neutron and synchrotron refinements data reveal that the crystal structure of $AgNbO_3$ has a distorted perovskite-type structure with the orthorhombic space group *Pmc*2_1 (no. 26) [21]. Figure 1 shows its crystal structure. The experimentally determined lattice parameters are a=15.64773 Å, b=5.55199 Å, c=5.60908 Å and α=β=γ=90° [22]. Niobium atoms form corner sharing NbO_6 octahedrons with adjacent oxygen atoms. The experimental crystal structure was optimised to obtain energy minimised structure and test the validity of the Buckingham potentials (refer to Table 1)[22-24], pseudopotentials and basis sets used in this study. The calculated structural parameters are in good agreement with corresponding experimental values as tabulated in Table 2.

2.2. Intrinsic defects

The diffusion of ions is influenced and/or mediated by intrinsic defects. These can be difficult to examine by experiment therefore here we calculated Schottky, Frenkel and anti-site defect energies using atomistic simulation. Isolated point defects (vacancy and interstitial) and appropriate lattice energies were combined to calculate Schottky and Frenkel defect energies. Using the Kröger-Vink notation [25] Frenkel, Schottky and anti-site defect reaction equations (Eqs.1-8) are written and shown below.

$$\text{Ag Frenkel: } \mathrm{Ag}_{\mathrm{Ag}}^{\mathrm{X}} \rightarrow V_{\mathrm{Ag}}' + \mathrm{Ag}_{\mathrm{i}}^{\bullet} \quad (1)$$

$$\text{O Frenkel: } \mathrm{O}_{\mathrm{O}}^{\mathrm{X}} \rightarrow V_{\mathrm{O}}^{\bullet\bullet} + \mathrm{O}_{\mathrm{i}}'' \quad (2)$$

$$\text{Nb Frenkel: } \mathrm{Nb}_{\mathrm{Nb}}^{\mathrm{X}} \rightarrow V_{\mathrm{Nb}}''''' + \mathrm{Nb}_{\mathrm{i}}^{\bullet\bullet\bullet\bullet\bullet} \quad (3)$$

$$\text{Schottky: } Ag_{Ag}^{X} + Nb_{Nb}^{X} + 3\,O_{O}^{X} \rightarrow V_{Ag}' + V_{Nb}''''' + 3\,V_{O}^{\bullet\bullet} + AgNbO_3 \quad (4)$$

$$Ag_2O \text{ Schottky: } Ag_{Ag}^{X} + O_{O}^{X} \rightarrow 2\,V_{Ag}' + V_{O}^{\bullet\bullet} + Ag_2O \quad (5)$$

$$Nb_2O_5 \text{ Schottky: } 2\,Nb_{Nb}^{X} + 5\,O_{O}^{X} \rightarrow 2\,V_{Nb}''''' + 5\,V_{O}^{\bullet\bullet} + Nb_2O_5 \quad (6)$$

$$\text{Ag/Nb antisite (isolated): } Ag_{Ag}^{X} + Nb_{Nb}^{X} \rightarrow Ag_{Nb}'''' + Nb_{Ag}^{\bullet\bullet\bullet\bullet} \quad (7)$$

$$\text{Ag/Nb antisite (cluster): } Ag_{Ag}^{X} + Nb_{Nb}^{X} \rightarrow \{Na_{Nb}'''' : Nb_{Ag}^{\bullet\bullet\bullet\bullet}\}^{X} \quad (8)$$

The calculated defect reaction energies are reported in Table 3. The lowest defect energy process is the Ag Frenkel (equation 1). This process would facilitate the formation of Ag vacancies required for the vacancy assisted Ag diffusion in $AgNbO_3$. The second most favourable defect process is the Ag_2O Schottky-like reaction (equation 5) which will ensure the formation of V_{Ag}' and $V_O^{\bullet\bullet}$ leading to the loss of Ag_2O. However, this process will be important at elevated temperatures. The Ag-Nb anti-site defect cluster (equation 8) energy is calculated to be 3.80 eV/defect meaning that this disorder will be present at very low concentration. This is due to high charge difference between Ag^+ and Nb^{5+} ions. The cluster form of anti-site defect is more stable than its isolated form by 3.81 eV. This is due to the aggregation of isolated defects forming defect cluster. The O Frenkel defect energy is 5.05 eV suggesting that this defect will not be significantly present in $AgNbO_3$. Other Schottky and Frenkel defect energies are relatively high meaning that they are highly unlikely to form at room temperature. Particularly, the Nb Frenkel energy is 16.16 eV showing the inefficacy of forming Nb^{5+} ion in the lattice.

2.3. Self-diffusion of silver and oxygen ions

In this section, we discuss the intrinsic silver and oxygen ion diffusion in $AgNbO_3$. In general, it is difficult to observe ion transport pathways and calculate

activation energies experimentally. Classical simulation allowed us to identify the possible diffusion paths together with activation energies. This simulation technique has been successfully applied to various oxide materials for validating experimentally reported migration pathways and predicting possible pathways for materials which do not have any experimental information [26-29]. For example, there was an excellent agreement between calculated and experimental Li-ion diffusion paths in $LiFePO_4$ [30,31]

Two different Ag local hops (A and B) were identified (refer to Figure 2). Calculated activation energies for each individual local hops with Ag-Ag distances are reported in Table 4. Figure 2 shows the energy profile diagrams for each local hops. Possible long-range diffusion paths were constructed using local hops. Three possible paths were identified. In the first long-range path (A→A→A→A), the Ag-ion migrates along the *a* axis in a linear fashion with an activation energy of migration of 2.42 eV. The second path (B→B→B→B) consists of local hops B only and silver ion migrates in a zig-zag pattern in the *bc* plane. The activation energy for this path is 2.44 eV. In the third path, Ag ion can use both local hops A and B in different ways with the overall action energy of 2.44 eV. Nevertheless, in all three paths, activation energies for Ag^+ ion migration are high implying that Ag^+ ion diffusion is slow in this material.

Thereafter, the possible local oxygen diffusion hops (P, Q, R, S and T) with their corresponding bond distances (see Table 5) were identified and their activation energies calculated. Long-range diffusion paths were constructed connecting local hops as shown in Figure 3 (a-b). Local hops P, Q and R have similar and low activation energies of 1.07 eV, 1.05 eV and 1.08 eV respectively. This is due to their bond distances closer to each other. Higher activation energies are calculated for hops S and T due to their longer bond distances. Energy profile diagrams are shown in figure

3 (c-g). There are three possible long-range paths present. In the first migration path (P→P→P→P), oxygen ions move along the *c* axis in a zig-zag pattern (refer to Figure 3a) with the activation energy of 1.07 eV. The second migration path (Q→R→Q→R) consists of local hops Q and R and oxygen ion moves along the *b* axis with a zig-zag pattern and the activation energy of 1.08 eV. Diffusion in the third path (S→T→S→T) is linear along the *a* axis with the activation energy of 3.72 eV. The activation energy of 1.07 eV for oxygen ion migration shows that $AgNbO_3$ can be considered as a good oxygen-ion conductor.

2.4. Solution of dopants

As substitution with dopants influences the materials performance, divalent, trivalent and tetravalent cation dopants were considered with appropriate charge compensating mechanism. Classical simulations allowed to screen a variety of dopants and predict promising dopants that can be tested experimentally. In all cases, lattice energies of dopant oxides were calculated and incorporated in the reaction equations. Buckingham potentials used for dopants are provided in the supplementary data (refer to Table S1).

2.4.1. Isovalent dopants

Initially we considered monovalent and pentavalent dopants on the Ag and Nb sites respectively. In the monovalent doping process, the silver site was populated with dopants having the same charge (M = Li, Na, K and Rb). This doping process can be described by the following reaction

$$M_2O + 2\,Ag_{Ag}^{X} \rightarrow 2M_{Ag}^{X} + Ag_2O \quad (9)$$

Figure 4 shows the solution enthalpies of M_2O. The results reveal that sodium is the most favourable dopant on the Ag site, having the lowest solution enthalpy of 0.41 eV to integrate into the lattice. This can be due to the ionic radius of Na^+ (1.18 Å),

which is close to that of Ag^+ (1.28 Å). The second most favourable dopant is the Li and its solution energy is 1.56 eV. Solution energy for K_2O differs only by 0.41 eV from that calculated for Li_2O. The highest solution energy of 3.58 eV is calculated for Rb_2O suggesting that this process *via* doping of Rb is unlikely to occur. Experimental studies on Na and Li doping on the Ag site of $AgNbO_3$ have been reported in order to increase the polarisation *via* distorting the crystal structure [32].

Doping on the Nb site was also considered. Here we only considered Ta^{5+} as a possible pentavalent cation. Reaction energy equation is described in equation 10.

$$Ta_2O_5 + 2\,Nb_{Nb}^{X} \rightarrow 2Ta_{Nb}^{x} + Nb_2O_5 \quad (10)$$

Solution energy for this process is 0.23 eV meaning that Ta is a promising dopant for this process. This is due to the ionic radius of Nb in an octahedral environment closely matches with that of Ta. The promising nature of this dopant is further confirmed by many experimental studies that reported the preparation of $AgTa_xNb_{1-x}O_3$ composites for use in high frequency applications [33,34].

2.4.2. Aliovalent dopants

2.4.2.1. Divalent dopants

Doping of divalent dopants (Mn, Ni, Zn, Co, Ca, Sr and Ba) on the Ag site can introduce additional silver vacancies, which are required for the vacancy mediated Ag-diffusion. The following reaction equation was used to calculate solution energies.

$$MO + 2\,Ag_{Ag}^{X} \rightarrow M_{Ag}^{\bullet} + V_{Ag}^{\prime} + Ag_2O \quad (11)$$

The lowest solution energy is calculated for Ca (see Figure 5). The solution energy calculated for Sr is only higher by 0.15 eV compared to that of Ca. The favourability of these two dopants is due to the ionic radius of Ag^+ (1.28 Å) closer to the ionic radii of both Ca^{2+} (1.12 Å) and Sr^{2+} (1.26 Å). Both Sr and Ca dopants have

been used experimentally to increase the energy storage property in $AgNbO_3$ [35]. Solution energies of other dopants are quite high because of their ionic radii deviating significantly from the ionic radius of Ag^+. The highest solution energy is reported for Ba^{2+} (5.85 eV).

2.4.2.2. Trivalent dopants

As discussed above, the formation of silver vacancies are necessary to enhance the vacancy mediated silver migration. The doping of trivalent cations (Al^{3+}, Ga^{3+}, Sc^{3+}, Y^{3+}, Gd^{3+} and La^{3+}) on the Ag site can double the concentration of vacancies compared to the doping of divalent cations on the same site (refer to equation 12).

$$M_2O_3 + 6\,V_V^X \rightarrow 2\,M_{Ag}^{\bullet\bullet} + 4\,V'_{Ag} + 3\,Ag_2O \qquad (12)$$

The most favourable dopant for this process is Gd^{3+} (see Figure 6). The solution energy for La is higher only by 0.04 eV compared to that calculated for Gd. There is a slight increase in the solution energy by 0.16 eV for Y. Favourable solution energies for these three dopants are due to their ionic radii, which are close to the ionic radius of Ag^+. The synthesis of Gd-doped $AgNbO_3$ has been reported and it is shown that the doped composites enhances the energy storage performance and the anti-ferroelectricity [36]. The solid–state–reaction method has been used to prepare La-doped $AgNbO_3$ samples and the enhancement in the photocatalytic activity compared to its un-doped samples has been reported by Li *et al*. [11]. Smaller ionic radius results in higher solution enthalpy. Doping of Al on the Ag site is highly unfavourable.

2.4.2.3. Tetravalent dopants

Finally, tetravalent dopants were considered on the Nb site. Two different charge compensating defects were considered. In the first mechanism, doping required Ag interstitials as charge compensating defects as shown in the equation 13.

$$2\,MO_2 + 2\,Nb_{Nb}^{X} + Ag_2O \rightarrow 2\,M'_{Nb} + 2\,Ag_i^{\bullet} + Nb_2O_5 \qquad (13)$$

Calculation shows that the most favourable dopant for this process is Ge^{4+} (refer to Figure 7a). Solution energy is 0.37 eV higher for Sn than that calculated for Ge. Both Ti and Zr exhibit almost similar solution energy that is 0.64 eV higher than that calculated for Ge. The ionic radius of Nb^{5+} is 0.64 Å. The favourability of these four dopants is partly due to their ionic radii that is only deviating slightly from the ionic radius of Nb^{5+}. The highest solution energy (5.36 eV) calculated for Si is due to its ionic radius deviating significantly (by 0.24 Å) from the ionic radius of Nb^{5+}.

In the second mechanism, oxygen vacancies were considered as charge compensating defects as shown in the equation 14. The formation of oxygen vacancies is anticipated to ease the loss of Ag_2O as the Ag Frenkel is the lowest defect energy process in $AgNbO_3$.

$$2\,MO_2 + 2\,Nb_{Nb}^{X} + Ag_2O \rightarrow 2\,M'_{Nb} + V_O^{\bullet\bullet} + Nb_2O_5 \qquad (14)$$

The same trend as noted in the first mechanism is observed (refer to Figure 7b). However, the solution energies are higher than those calculated in the first mechanism. This indicates that the formation of silver interstitials is easier than that of oxygen vacancies upon doping of tetravalent cations on the Nb site in $AgNbO_3$.

2.5. Electronic structures of un-doped and doped $AgNbO_3$

Density functional theory (DFT) calculations were performed to examine the chemical environment of dopants and electronic structures of doped configurations. The results obtained for the most favourable dopants are discussed here.

In the Na-doped configuration, Na-O bond distances are slightly shorter than the Ag-O bond distance calculated in the un-doped $AgNbO_3$ (refer to Figure 8). This is due to the small difference in the ionic radius between Na^+ and Ag^+ as discussed in

the section 2.4.1. Density of states (DOS) plot shows that $AgNbO_3$ is a semiconductor with the band gap of 1.80 eV (refer to Figure 9a). The calculated band gap value underestimates the experimentally observed band gap of 2.80 eV [37]. The underestimation is due to the fact that GGA-PBE functional does not describe the self-interaction adequately. A plane wave based DFT calculation with local density approximation also underestimates the experimental band gap by 1.30 eV [38]. The doping of Na does not alter the Fermi energy level significantly and a slight reduction in the band gap by 0.2 eV is observed (refer to Figure 9b). Atomic DOS of Na shows the absence of additional peaks arising from Na in the band gap region (refer to Figure 9g.

The Ca-O bond distances are slightly shorter than Ag-O bond distances (refer to Figure 8c) because of the higher charge density of Ca^{2+} (smaller ionic radius and higher charge) than that of Ag^{+}. There is a significant shift in the Fermi energy level upon Ca doping (refer to Figure 9c). Fermi level shifts towards the conduction band by 2.30 eV and the band gap is reduced by 0.40 eV. The band gap region does not have any states arising from Ca (refer to Figure 9h).

In the Gd-doped configuration, Gd-O bond distances are shorter than the Ag-O bond distance (refer to Figure 8d). This is due to the smaller ionic radius of Gd^{3+} (1.05 Å) and higher charge of Gd (+3) than that of Ag^{+} (1.28 Å) and Ag (+1), respectively. The band gap reduces by ~0.4 eV and the Fermi level shifts towards conduction band upon Gd doping (refer to Figure 9i).

The doping of Ge on the Nb site has a distorted GeO_6 octahedron with longer bond distances than that observed in the NbO_6 octahedron (refer to Figure 8f). This is mainly due to the smaller charge of Ge (+4) than that of Nb (+5). There is a significant shift in the Fermi energy level by ~1 eV towards the valence band and the band gap is

reduced by ~0.4 eV upon doping (refer to Figure 9e) The *s* and *p* states of Ge appear at 3 eV in valence band (refer to Figure 9j).

Finally, the electronic structure of Ta-doped $AgNbO_3$ is discussed. A distorted TaO_6 octahedron is shown in Figure 8g. Though both Nb and Ta exhibit +5 charge, the longer Ta-O distances and distortion of TaO_6 should be from their different electronic configurations and atomic radii. The Fermi energy level shifts by 0.8 eV towards the conduction band and the doped structure becomes metallic (refer to Figure 9f). The metallic nature of doped configuration should be due to the distortion in the lattice as there is no contribution from Ta states in the band gap region (refer to Figure 9k).

The calculation results showed that doping has an obvious effect on the electronic structures. Therefore, the doping could influence the transport properties of $AgNbO_3$. As practical applications depends on the transport property, there is a necessity for future experimental studies.

3. Conclusions

Computational modelling techniques were applied to examine the defect chemistry, diffusion of silver and oxygen ions, solution of dopants and electronic structures of doped configurations in $AgNbO_3$. The most energetically favourable defect is the Ag Frenkel ensuring the formation of Ag vacancies required for the vacancy assisted Ag diffusion. The diffusion of oxygen in this material is faster than that of silver. The favourable isovalent dopants are Na and Ta on the Ag and Nb sites respectively. The tetravalent dopant Ge^{4+} on the Nb site would increase the concentration of oxygen vacancies needed for the oxygen migration and the concentration of Ag in the form of Ag interstitials. The doping of Ca on the Ag site would increase the concentration of Ag vacancies required for the self-diffusion of Ag in $AgNbO_3$.

4. Computational Methods

Atomistic simulation based on the classical potentials as implemented in the GULP (General Utility Lattice Program) code [39] was applied to examine the defect energetics, Ag and O ion migration pathways together with activation energies and solution of a variety of dopants. Interactions between ions were modelled using Coulombic attractions and short-range interactions (Pauli repulsion and van der Waals dispersive attraction). Short-range interactions were modelled using Buckingham potentials (Table 1). The Broyden-Fletcher-Goldfarb-Shanno (BFGS) algorithm [40] was used to relax ionic positions and lattice constants. A gradient norm of 0.001 eV/Å was used to converge all configurations. Point defects and migrating ions were modelled using Mott-Littleton method [41]. The activation energy of migration is defined as the local maximum energy along the lowest energy diffusion path. Current model assumes that ions are in their full charge within dilute limit overestimating defect energies [42]. However, it is anticipated that the trend will be consistent.

A plane wave DFT code VASP (Vienna Ab initio Simulation Package) [43] was used to calculate the electronic structures of both non-defective and doped $AgNbO_3$. A 1×2×2 supercell containing 160 atoms was used to model doped $AgNbO_3$. In all cases a single dopant was considered. Projected Augment Wave (PAW) pseudo-potentials [44] as stored in the VASP potential library were used. In all calculations, a plane wave basis set with a cut-off of 500 eV was used. The generalized gradient approximation (GGA) as parameterized by Perdew, Burke and Ernzerhof (PBE) [45] was applied to model the exchange-correlation effects. All structures were relaxed using the conjugate gradient algorithm [46]. A force tolerance value of 0.001 eV/Å was used to obtain energy minimized structures. A 2×6×6 Monkhorst-Pack [47] k-point mesh which yielded 32 k-points was used in all calculations.

5. Acknowledgements

We thank High Performance Computing Centers at Coventry University and Imperial College London for providing computational facilities and support.

References

[1] P. K. Panda, *Journal of Materials Science* **2009**, *44*, 5049-5062.
[2] P. K. Panda, B. Sahoo, *Ferroelectrics* **2015**, 474, 128-143.
[3] M. E. Lines, A. M. Glass, Principles and Applications of Ferroelectrics and Related Materials, Oxford University Press, Oxford, **2001**.
[4] B. Jaffe, W. R. Cook, H. Jaffe, in Piezoelectric Ceramics (Eds.: B. Jaffe, W. R. Cook, H. Jaffe), Academic Press, **1971**, pp. 1-5.
[5] J. F. Scott, Ferroelectric Memories, Springer Berlin Heidelberg, **2013**.
[6] D. Fu, M. Endo, H. Taniguchi, T. Taniyama, M. Itoh, S.-y. Koshihara, *Journal of Physics: Condensed Matter* **2011**, 23, 075901.
[7] S. Miga, A. Kania, J. Dec, *Journal of Physics: Condensed Matter* 2011, 23, 155901.
[8] J. Gao, Y. Zhang, L. Zhao, K.-Y. Lee, Q. Liu, A. Studer, M. Hinterstein, S. Zhang, J.-F. Li, *Journal of Materials Chemistry A* **2019**, 7, 2225-2232.
[9] D. Fu, M. Itoh, S.-y. Koshihara, *Journal of Applied Physics* **2009**, 106, 104104.
[10] L. Yang, J. Liu, H. Chang, S. Tang, *RSC Advances* **2015**, 5, 59970-59975.
[11] G. Li, T. Kako, D. Wang, Z. Zou, J. Ye, *Dalton Transactions* **2009**, 2423-2427.
[12] Y. Tian, L. Jin, Q. Hu, K. Yu, Y. Zhuang, G. Viola, I. Abrahams, Z. Xu, X. Wei, H. Yan, *Journal of Materials Chemistry A* **2019**, 7, 834-842.
[13] E. E. Jay, M. J. D. Rushton, A. Chroneos, R. W. Grimes, J. A. Kilner, *Physical Chemistry Chemical Physics* **2015**, 17, 178-183.
[14] J. Zhu, M. Vasilopoulou, D. Davazoglou, S. Kennou, A. Chroneos, U. Schwingenschlögl, *Scientific Reports* **2017**, 7, 40882.
[15] N. Kuganathan, A. Kordatos, M. E. Fitzpatrick, R. V. Vovk, A. Chroneos, *Solid State Ionics* **2018**, 327, 93-98.
[16] M. S. Islam, C. A. J. Fisher, *Chemical Society Reviews* **2014**, 43, 185-204.
[17] N. Kuganathan, L. H. Tsoukalas, A. Chroneos, *Solid State Ionics* **2019**, 335, 61-66.
[18] N. Kuganathan, P. Iyngaran, R. Vovk, A. Chroneos, *Scientific Reports* **2019**, 9, 4394.
[19] N. Kuganathan, A. Chroneos, *Scientific Reports* **2019**, 9, 333.
[20] J. R. Tolchard, P. R. Slater, M. S. Islam, *Advanced Functional Materials* **2007**, 17, 2564-2571.
[21] M. Yashima, S. Matsuyama, R. Sano, M. Itoh, K. Tsuda, D. Fu, *Chemistry of Materials* **2011**, 23, 1643-1645.
[22] D.J.Binks, PhD Thesis, October **1994** University of Surrey, UK.
[23] M.S.Khan, PhD Thesis, January **1998** University of Surrey, UK.
[24] N. Kuganathan, A. Chroneos, *Energies* **2020**, 13, 1285.
[25] F. A. Kröger, H. J. Vink, in Solid State Physics, Vol. 3 (Eds.: F. Seitz, D. Turnbull), Academic Press, 1956, pp. 307-435.
[26] C. A. J. Fisher, N. Kuganathan, M. S. Islam, *Journal of Materials Chemistry A* **2013**, 1, 4207-4214.
[27] N. Kuganathan, A. Kordatos, A. Chroneos, *Scientific Reports* **2019**, 9, 550.
[28] N. Kuganathan, A. Kordatos, N. Kelaidis, A. Chroneos, *Scientific Reports* **2019**, 9, 2192.
[29] N. Kuganathan, A. Kordatos, S. Anurakavan, P. Iyngaran, A. Chroneos, *Materials Chemistry and Physics* **2019**, 225, 34-41.

[30] C. A. J. Fisher, V. M. Hart Prieto, M. S. Islam, *Chemistry of Materials* **2008**, 20, 5907-5915.
[31] S.-i. Nishimura, G. Kobayashi, K. Ohoyama, R. Kanno, M. Yashima, A. Yamada, *Nature Materials* **2008**, 7, 707.
[32] G. Li, T. Kako, D. Wang, Z. Zou, J. Ye, *Journal of Solid State Chemistry* **2007**, 180, 2845-2850.
[33] M. Valant, A.-K. Axelsson, B. Zou, N. M. Alford, *Journal of Optoelectronics and Advanced Materials* **2007**, 9, 1377-1381.
[34] P. Sciau, A. Kania, B. Dkhil, E. Suard, A. Ratuszna, *Journal of Physics: Condensed Matter* **2004**, 16, 2795-2810.
[35] K. Han, N. Luo, S. Mao, F. Zhuo, X. Chen, L. Liu, C. Hu, H. Zhou, X. Wang, Y. Wei, *Journal of Materiomics* **2019**, 5, 597-605.
[36] S. Li, H. Nie, G. Wang, C. Xu, N. Liu, M. Zhou, F. Cao, X. Dong, *Journal of Materials Chemistry C* **2019**, 7, 1551-1560.
[37] H. Kato, H. Kobayashi, A. Kudo, *The Journal of Physical Chemistry B* **2002**, 106, 12441-12447.
[38] C. Suleyman, S. Sevket, *Open Physics* **2008**, 6, 730-736.
[39] J. D. Gale, A. L. Rohl, *Molecular Simulation* **2003**, 29, 291-341.
[40] J. D. Gale, *Journal of the Chemical Society, Faraday Transactions* **1997**, 93, 629-637.
[41] N. F. Mott, M. J. Littleton, *Transactions of the Faraday Society* **1938**, 34, 485-499.
[42] R. W. Grimes, G. Busker, M. A. McCoy, A. Chroneos, J. A. Kilner, S.-P. Chen, *Berichte der Bunsengesellschaft für physikalische Chemie* **1997**, 101, 1204-1210.
[43] G. Kresse, J. Furthmüller, *Physical Review B* **1996**, 54, 11169-11186.
[44] P. E. Blöchl, *Physical Review B* **1994**, 50, 17953-17979.
[45] J. P. Perdew, K. Burke, M. Ernzerhof, *Physical Review Letters* **1996**, 77, 3865-3868.
[46] W. H. Press, S. A. Teukolsky, W. T. Vetterling, B. P. Flannery, Numerical recipes in C (2nd ed.): the art of scientific computing, Cambridge University Press, **1992**.
[47] H. J. Monkhorst, J. D. Pack, *Physical Review B* **1976**, 13, 5188-5.

Table 1. Buckingham potential parameters used in the classical simulations of $AgNbO_3$.

Two-body [Φ_{ij} (r_{ij}) = A_{ij} exp (− r_{ij} /ρ_{ij}) − C_{ij} / r_{ij}^6, where A, ρ and C are parameters which were selected carefully to reproduce the experimental data. The values of Y and K represent the shell charges and spring constants. A very large spring constant means there no shell charge and atom is treated as core. The different values of A are due to the attractive (Ag^+–O^{2-}) and repulsive (O^{2-}–O^{2-}) terms.] [22-24]

Interaction	***A* / eV**	***ρ* / Å**	***C* / eV·Å^6**	**Y / e**	**K / eV·Å^{-2}**
Ag^+–O^{2-}	1417.030	0.2851	0.000	1.000	99999
Nb^{5+} – O^{2-}	1796.30	0.34598	0.000	–4.497	1358.58
O^{2-}–O^{2-}	22764.30	0.1490	28.00	–2.811	103.07

Table 2. Calculated and experimental lattice parameters of orthorhombic $AgNbO_3$.

Parameter	Calculated		Experiment [21]	|Δ|(%)	
	Classical	DFT		Classical	DFT
a (Å)	15.65622	15.69857	15.64773	0.05	0.32
b (Å)	5.52531	5.62409	5.55199	0.48	1.30
c= (Å)	5.55070	5.71087	5.60908	1.04	1.81
α = β =γ (°)	90.00	90.00	90.00	0.00	0.00

Table 3. Reaction energies calculated for Schottky, Frenkel and anti-site defects

Defect process	equation	Reaction energy (eV)	Reaction energy (eV)/defect
Ag Frenkel	1	4.00	2.00
O Frenkel	2	10.10	5.05
Nb Frenkel	3	32.32	16.16
Schottky	4	24.65	4.93
Ag_2O Schottky	5	9.63	3.21
Nb_2O_5 Schottky	6	46.62	6.66
Ag/Nb anti-site (isolated)	7	15.22	7.61
Ag/Nb anti-site (cluster)	8	7.60	3.80

Table 4. Calculated Ag-Ag separations and activation energies for the Ag-ion migration between two adjacent Ag sites (refer to Figure 2).

Migration path	Ag–Ag separation (Å)	Activation energy (eV)
A	3.914	2.42
B	3.918	2.44

Table 5. Calculated O-O separations and activation energies for the O-ion migration between two adjacent O sites (refer to Figure 3).

Migration path	O–O separation (Å)	Activation energy (eV)
P	2.78328	1.07
Q	2.78882	1.05
R	2.79538	1.08
S	3.56961	3.09
T	4.26764	3.72

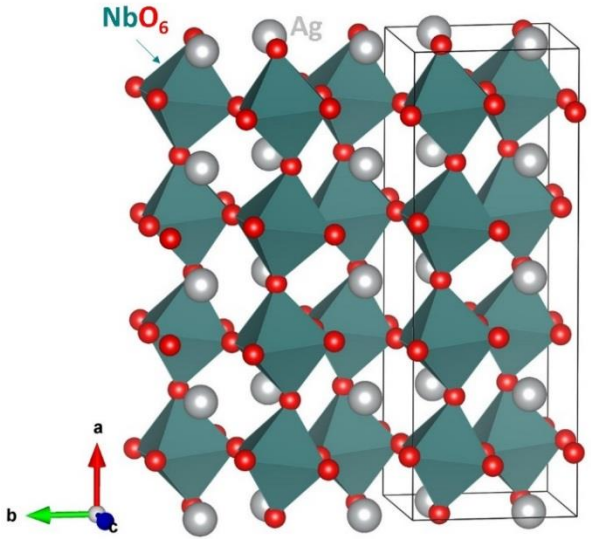

Figure 1. Crystal structure of orthorhombic $AgNbO_3$

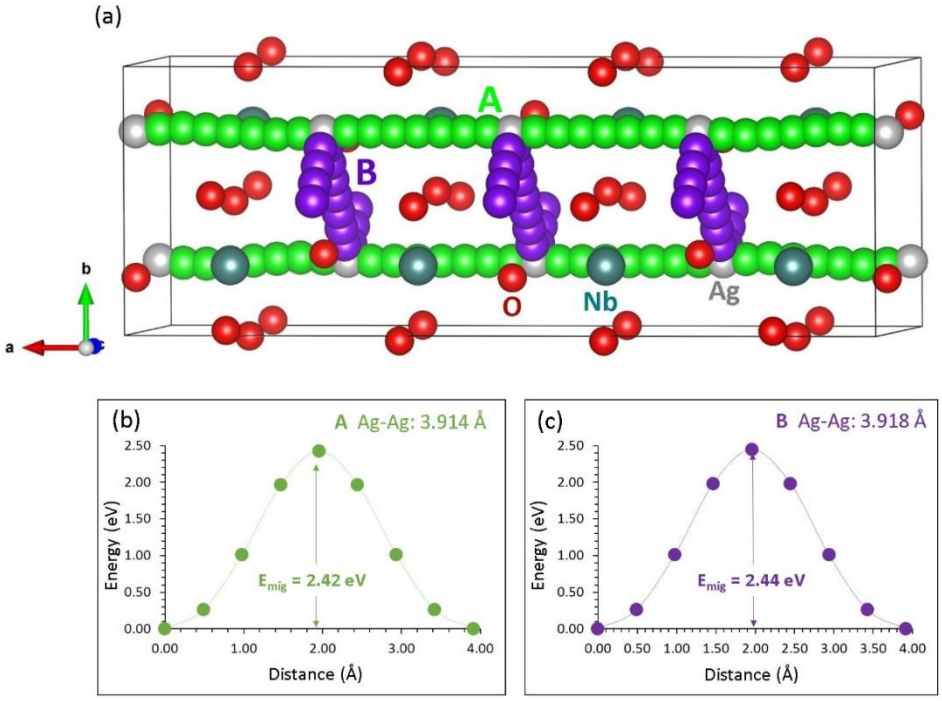

Figure 2. (a) Long range silver diffusion paths and (b-c) energy profile diagrams for the local Ag hops (A and B)

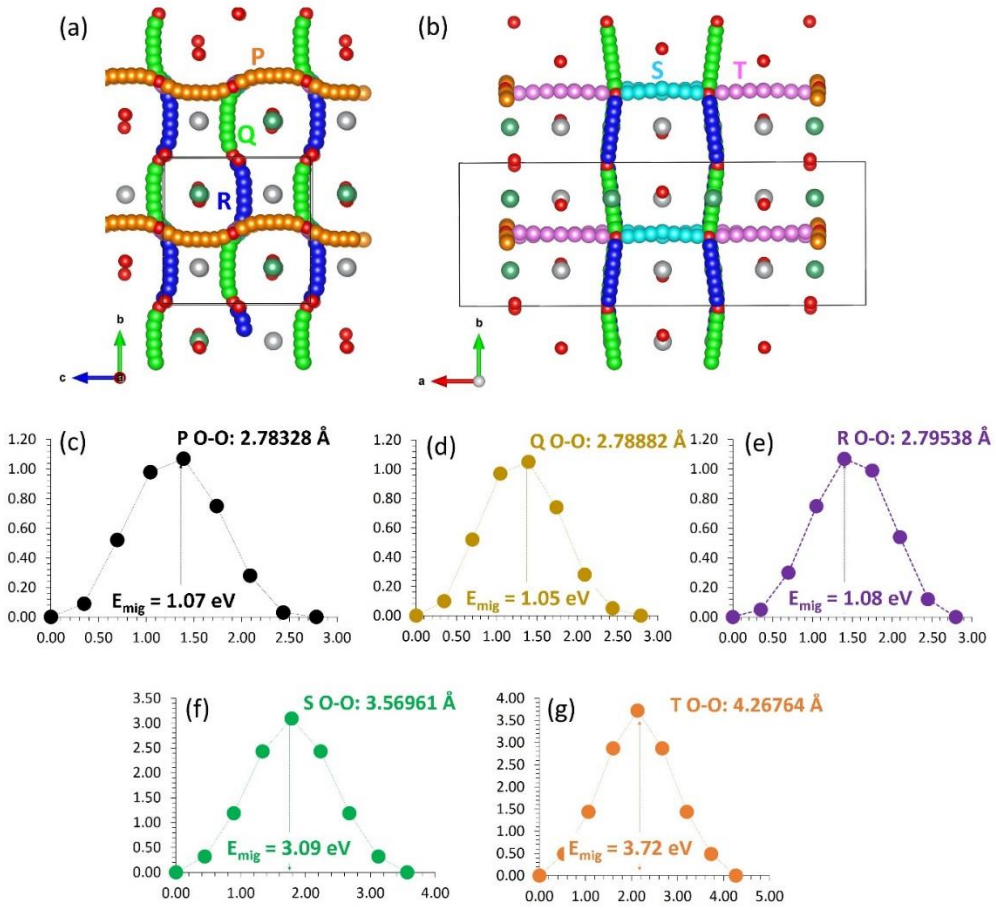

Figure 3. (a-b) Long range oxygen diffusion paths and (c-g) energy profile diagrams for the local O hops (P, Q, R, S and T).

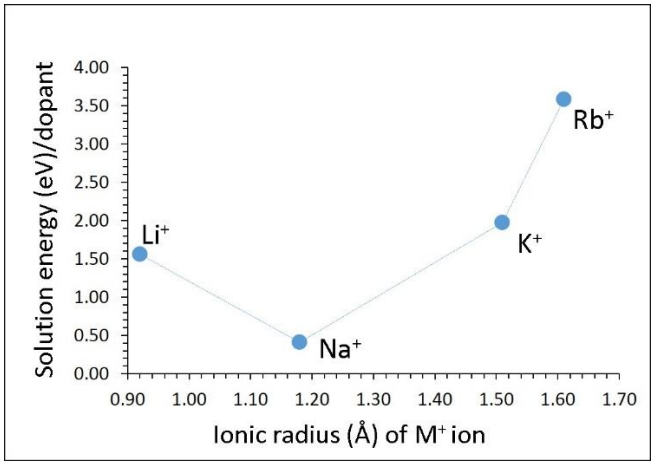

Figure 4. Calculated solution energies of M_2O (M=Li, Na, K and Rb) with respect to the M^+ ionic radius in $AgNbO_3$.

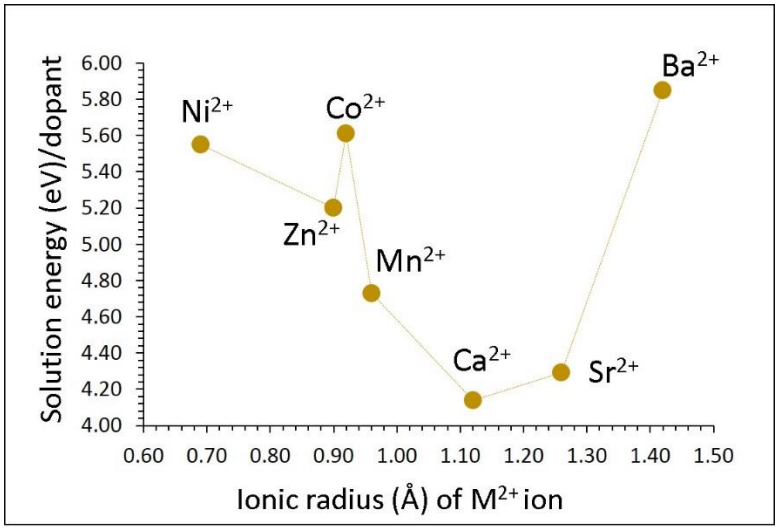

Figure 5. Calculated solution energies of MO (M=Mn, Ni, Zn, Co, Ca, Sr and Ba) with respect to the M^{2+} ionic radius in $AgNbO_3$.

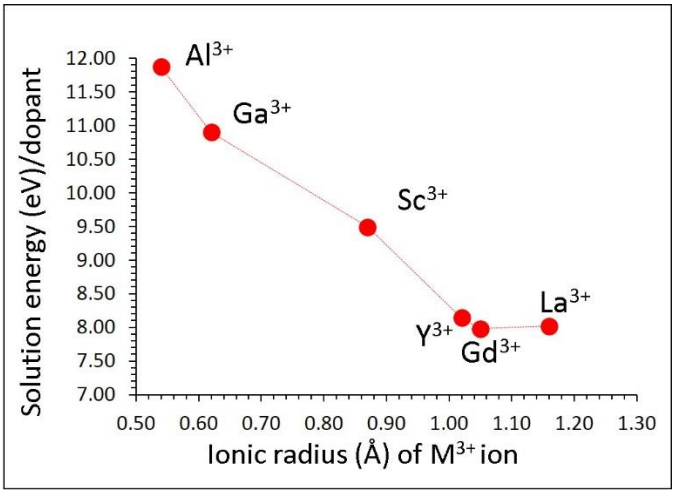

Figure 6. Calculated solution energies of M_2O_3 (M= Al, Ga, Sc, Y, Gd and La) with respect to the M^{3+} ionic radius in $AgNbO_3$.

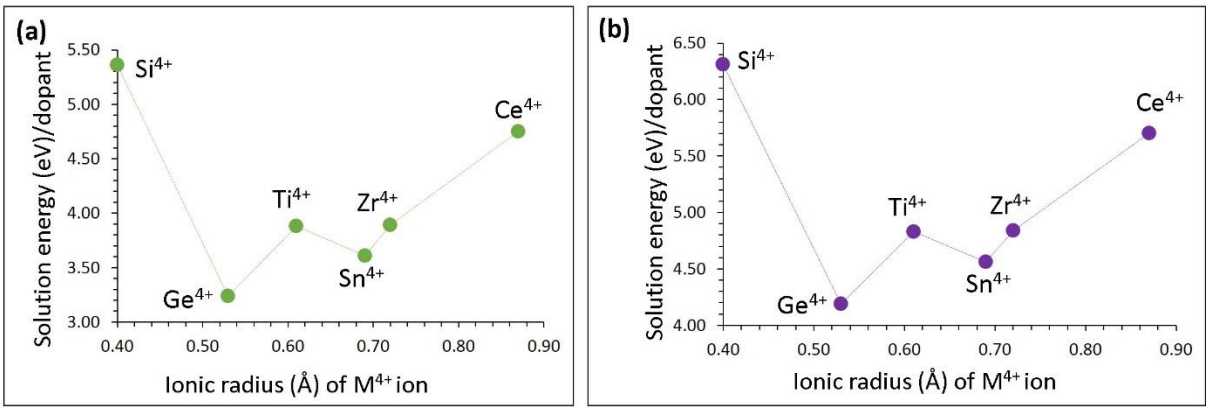

Figure 7. Calculated solution energies of MO_2 (M= Si, Ge, Ti, Sn, Zr and Ce) with (a) silver interstitials and (b) oxygen vacancies as charge compensating defects with respect to the M^{4+} ionic radius in $AgNbO_3$.

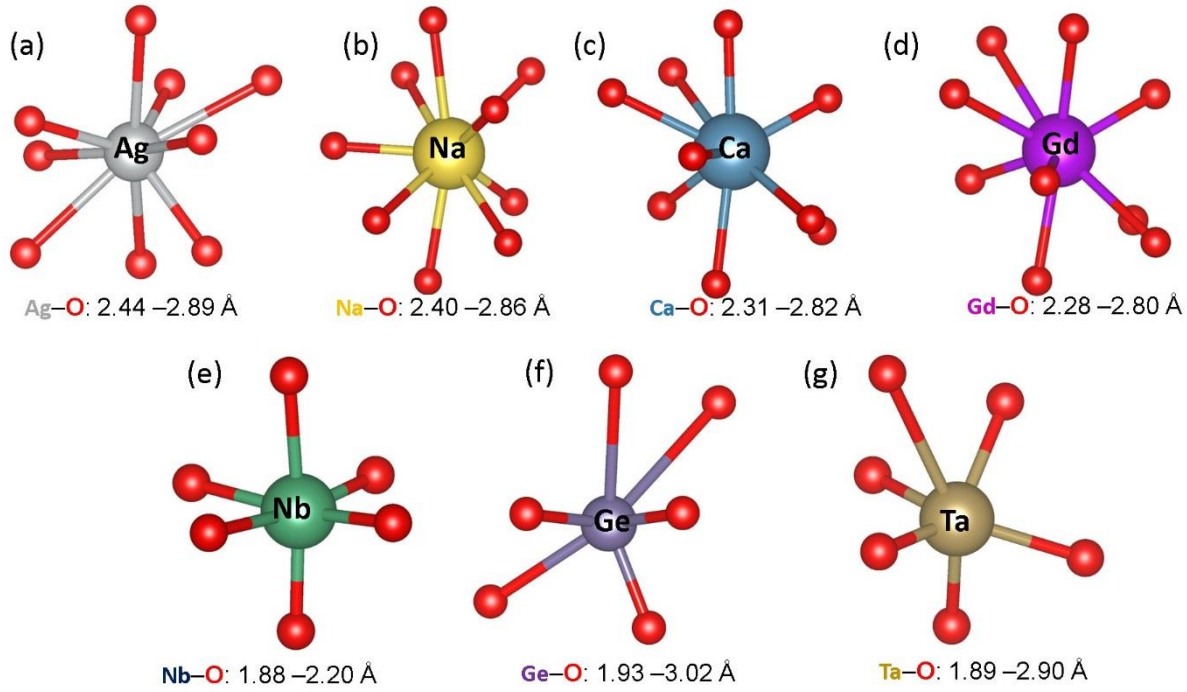

Figure 8. Optimised structures showing (a) Ag-O bond distances in the pristine $AgNbO_3$ structure, (b-d) dopant-oxygen bond distances for dopants substituted on the Ag site, (e) Nb-O bond distances in the pristine $AgNbO_3$ structure and (f-g) dopant-oxygen bond distances for dopants substituted on the Nb site.

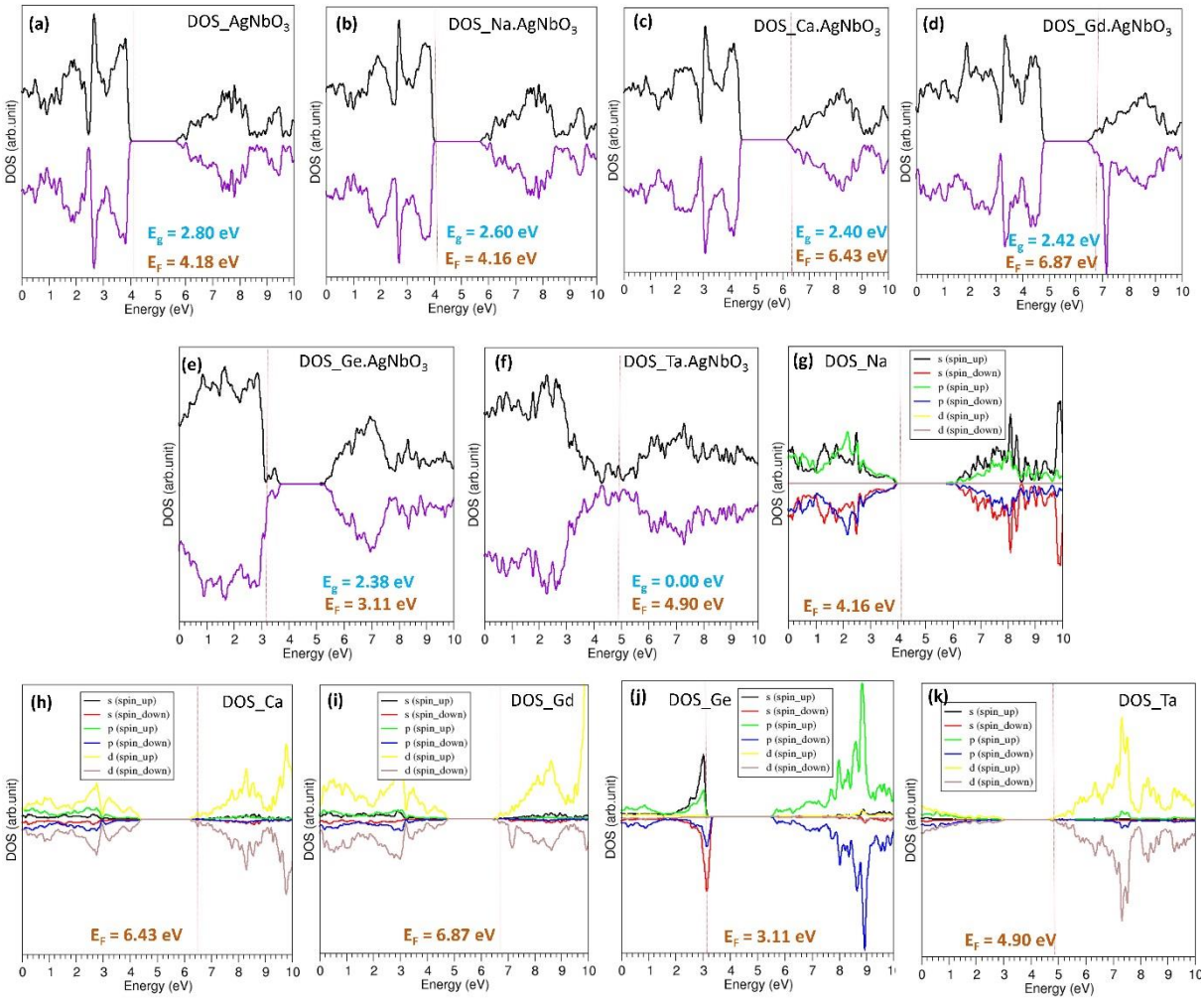

Figure 9. Total DOS plots of (a) un-doped $AgNbO_3$, (b-d) $AgNbO_3$ doped with Na, Ca and Gd on the Ag site respectively, (e-f) $AgNbO_3$ doped with Ge and Ta on the Nb site respectively and (g-k) atomic DOS plots of corresponding dopants (Na, Ca, Gd, Ge and Ta). Dot lines correspond to the Fermi energy level. Fermi energy (E_F) and band gap (E_g) values are also shown.

,